Enhanced nonlinear interaction in a microcavity under coherent excitation

Samuel Serna,[1,2] **Jérèmy Oden,**[1] **Marc Hanna,**[1] **Charles Caer,**[2] **Xavier Le Roux,**[2] **Christophe Sauvan,**[1] **Philippe Delaye,**[1] **Eric Cassan**[2] **and Nicolas Dubreuil**[1,*]

[1]*Laboratoire Charles Fabry, Institut d'Optique Graduate School, CNRS, Université Paris-Saclay, 91127 Palaiseau cedex, France*
[2]*Institut d' Électronique Fondamentale, Université Paris-Sud 11, CNRS UMR 8622, Bat. 220, 91405 Orsay Cedex, France*
[*]*nicolas.dubreuil@institutoptique.fr*

Abstract: The large field enhancement that can be achieved in high quality factor and small mode volume photonic crystal microcavities leads to strengthened nonlinear interactions. However, the frequency shift dynamics of the cavity resonance under a pulsed excitation, which is driven by nonlinear refractive index change, tends to limit the coupling efficiency between the pulse and the cavity. As a consequence, the cavity enhancement effect cannot last for the entire pulse duration, limiting the interaction between the pulse and the intra-cavity material. In order to preserve the benefit of light localization throughout the pulsed excitation, we report the first experimental demonstration of coherent excitation of a nonlinear microcavity, leading to an enhanced intra-cavity nonlinear interaction. We investigate the nonlinear behavior of a Silicon-based microcavity subject to tailored positively chirped pulses, enabling to increase the free carrier density generated by two-photon absorption by up to a factor of 2.5 compared with a Fourier-transform limited pulse excitation of equal energy. It is accompanied by an extended frequency blue-shift of the cavity resonance reaching 19 times the linear cavity bandwidth. This experimental result highlights the interest in using coherent excitation to control intra-cavity light-matter interactions and nonlinear dynamics of microcavity-based optical devices.

References and links

1. M. Soljacic and J. D. Joannopoulos, "Enhancement of nonlinear effects using photonic crystals," Nature Mater. **3**, 211–219 (2004).
2. K. Nozaki, T. Tanabe, A. Shinya, S. Matsuo, T. Sato, H. Taniyama, and M. Notomi, "Sub-femtojoule all-optical switching using a photonic-crystal nanocavity," Nat Photon **4**, 477–483 (2010).
3. Q. Xu and M. Lipson, "All-optical logic based on silicon micro-ring resonators," Opt. Express **15**, 924–929 (2007).
4. K. Nozaki, A. Shinya, S. Matsuo, Y. Suzaki, T. Segawa, T. Sato, Y. Kawaguchi, R. Takahashi, and M. Notomi, "Ultralow-power all-optical ram based on nanocavities," Nature Photon. **6**, 248–252 (2012).
5. T. Tanabe, M. Notomi, S. Mitsugi, A. Shinya, and E. Kuramochi, "All-optical switches on a silicon chip realized using photonic crystal nanocavities," Appl. Phys. Lett. **87**, 151112 (2005).

6. F. Raineri, C. Cojocaru, P. Monnier, A. Levenson, R. Raj, C. Seassal, X. Letartre, and P. Viktorovitch, "Ultrafast dynamics of the third-order nonlinear response in a two-dimensional inp-based photonic crystal," Appl. Phys. Lett. **85**, 1880–1882 (2004).
7. C. Husko, A. De Rossi, S. Combrie, Q. V. Tran, F. Raineri, and C. W. Wong, "Ultrafast all-optical modulation in GaAs photonic crystal cavities," Appl. Phys. Lett. **94**, 021111 (2009).
8. V. Eckhouse, I. Cestier, G. Eisenstein, S. Combrié, G. Lehoucq, and A. D. Rossi, "Kerr-induced all-optical switching in a gainp photonic crystal fabry-perot resonator," Opt. Express **20**, 8524–8534 (2012).
9. Z. K. Ioannidis, P. M. Radmore, and I. P. Giles, "Dynamic response of an all-fiber ring resonator," Opt. Lett. **13**, 422–424 (1988).
10. Y. Dumeige, S. Trebaol, L. Ghişa, T. K. N. Nguyên, H. Tavernier, and P. Féron, "Determination of coupling regime of high-q resonators and optical gain of highly selective amplifiers," J. Opt. Soc. Am. B **25**, 2073–2080 (2008).
11. D. Vujic and S. John, "Pulse reshaping in photonic crystal waveguides and microcavities with kerr nonlinearity: Critical issues for all-optical switching," Phys. Rev. A **72**, 013807 (2005).
12. W. V. Sorin and R. S. Tucker, "Optical pulse storage, shaping, and wavelength conversion in resonators with controllable input coupling," J. Lightwave Technol. **27**, 2587–2594 (2009).
13. S. Sandhu, M. L. Povinelli, and S. Fan, "Enhancing optical switching with coherent control," Appl. Phys. Lett. **96**, 231108 (2010).
14. D. Meshulach and Y. Silberberg, "Coherent quantum control of two-photon transitions by a femtosecond laser pulse," Nature **396**, 239–242 (1998).
15. A. Weiner, "Femtosecond pulse shaping using spatial light modulators," Rev. Sci. Instrum. **71**, 1929 (2000).
16. S. Zamith, J. Degert, S. Stock, B. de Beauvoir, V. Blanchet, M. Aziz Bouchene, and B. Girard, "Observation of coherent transients in ultrashort chirped excitation of an undamped two-level system," Phys. Rev. Lett. **87**, 033001 (2001).
17. P. Trøst Kristensen, M. Heuck, and J. Mørk, "Optimal switching using coherent control," Appl. Phys. Lett. **102**, 041107 (2013).
18. J. Oden, S. Trebaol, P. Delaye, and N. Dubreuil, "Coherent excitation of a nonlinear microcavity," J. Eur. Opt. Soc.-Rapid **8**, 13046 (2013).
19. P. Velha, J. C. Rodier, P. Lalanne, J. P. Hugonin, D. Peyrade, E. Picard, T. Charvolin, and E. Hadji, "Ultracompact silicon-on-insulator ridge-waveguide mirrors with high reflectance," Appl. Phys. Lett. **89**, 171121 (2006).
20. P. Velha, J. C. Rodier, P. Lalanne, J. P. Hugonin, D. Peyrade, E. Picard, T. Charvolin, and E. Hadji, "Ultra-high-reflectivity photonic-bandgap mirrors in a ridge soi waveguide," New Journal of Physics **8**, 204 (2006).
21. E. Silberstein, P. Lalanne, J.-P. Hugonin, and Q. Cao, "Use of grating theories in integrated optics," J. Opt. Soc. Am. A **18**, 2865–2875 (2001).
22. A. C. Turner, C. Manolatou, B. S. Schmidt, M. Lipson, M. A. Foster, J. E. Sharping, and A. L. Gaeta, "Tailored anomalous group-velocity dispersion in silicon channel waveguides," Opt. Express **14**, 4357–4362 (2006).
23. P. Barclay, K. Srinivasan, and O. Painter, "Nonlinear response of silicon photonic crystal microresonators excited via an integrated waveguide and fiber taper," Opt. Express **13**, 801–820 (2005).
24. O. Martinez, "3000 times grating compressor with positive group velocity dispersion: Application to fiber compensation in 1.3-1.6 μm region," IEEE J. Quantum Electron. **23**, 59 – 64 (1987).
25. V. R. Almeida, C. A. Barrios, R. R. Panepucci, and M. Lipson, "All-optical control of light on a silicon chip," Nature **431**, 1081–1084 (2004).
26. M. Castellanos Muñoz, A. Y. Petrov, and M. Eich, "All-optical on-chip dynamic frequency conversion," Appl. Phys. Lett. **101**, 141119 (2012).
27. J. Bravo-Abad, S. Fan, S. G. Johnson, J. D. Joannopoulos, and M. Soljačić, "Modeling nonlinear optical phenomena in nanophotonics," J. Lightwave Technol. **25**, 2539–2546 (2007).
28. R. S. Judson and H. Rabitz, "Teaching lasers to control molecules," Phys. Rev. Lett. **68**, 1500 (1992).
29. E. Kuramochi, K. Nozaki, A. Shinya, K. Takeda, T. Sato, S. Matsuo, H. Taniyama, H. Sumikura, and M. Notomi, "Large-scale integration of wavelength-addressable all-optical memories on a photonic crystal chip," Nature Photon. **8**, 474–481 (2014).
30. C. Froehly, B. Colombeau, and M. Vampouille, "Shaping and analysis of picosecond light pulses," in "Progress in Optics," , vol. 20, E. Wolf, ed. (North–Holland, 1983), pp. 65–153.
31. G. P. Agrawal, *Applications of Nonlinear Fiber Optics* (Academic Press, 2008), chap. 6, pp. 245–300, 2nd ed.
32. Q. Lin, O. J. Painter, and G. P. Agrawal, "Nonlinear optical phenomena in silicon waveguides: Modeling and applications," Opt. Express **15**, 16604–16644 (2007).
33. A. Baron, A. Ryasnyanskiy, N. Dubreuil, P. Delaye, Q. V. Tran, S. Combrié, A. de Rossi, R. Frey, and G. Roosen, "Light localization induced enhancement of third order nonlinearities in a gaas photonic crystal waveguide," Opt. Express **17**, 552–557 (2009).

1. Introduction

The strong light confinement achieved in photonic crystal structures allows the enhancement of light-matter interactions, including nonlinear effects [1]. Recent developments of all-optical nonlinear functions, like optical switches [2], NAND gates [3] or all-optical random access memories [4], based on photonic crystal cavities rely on their very high ratio between the quality factor Q and the mode volume V. The consecutive strong enhancement of field intensity inside the cavity allows the realization of nonlinear functions with very-low control energy [2, 4]. However, the field enhancement taking place inside high-Q microcavities necessarily restricts the signal bandwidth and the amount of energy that can be transferred between the control pulse and the intra-cavity material.

As an illustration, we consider the operation of all-optical switches based on nonlinear photonic crystal microcavities under the control of a resonant pulse, which have been demonstrated in Silicon [5], InP [6] (containing quantum wells), GaAs [7], InGaAsP [2], and GaInP [8]. These all-optical devices based on semiconductor microcavities rely on nonlinear refractive index dynamic change induced by a control pulse, which in turns shifts the frequency of the cavity resonance, inducing a modification of the cavity transmission for incoming optical signal. The induced refractive index changes in these materials are mainly driven by optical Kerr effect and by free carriers generated by either one-photon absorption or two-photon absorption. Although nonlinear refractive effects induce the switching operation, the imparted frequency shift dynamics of the cavity resonance, which is activated by the front edge of the control pulse, tends to limit the coupling efficiency of the rest of the pulse. As a result, the cavity enhancement effect is not maintained for the entire control pulse duration, even if the latter is longer than the cavity photon lifetime, thereby limiting the energy transfer between the control pulse and the intra-cavity material. In addition, the mismatch between the drifting cavity resonance frequency and the frequency content of the control pulse leads to ringing behavior [9, 10], inducing temporal distorsion on the signal pulse [11].

In order to better control the pulse excitation of an optical resonance, the ideas of controlling either the coupling relationship into micro-resonators in relation with the pulse shape [12] or the pulse shape itself in relation with the temporal behavior of the intra-cavity amplitude field [13] have been theoretically investigated. The latter consists in transposing pulse shaping techniques that are routinely used to coherently excite atomic or molecular transitions in order to control light matter interactions [14–16]. In [13], the authors show with numerical simulations that a pulse with a controlled spectral phase relationship, compensating for the linear dispersion of the cavity resonance, can reduce the switching threshold power of a bistable Kerr microcavity. A controlled two-pulse excitation scheme of a pure-Kerr microcavity has also been theoretically investigated in [17]. While these works deal with the behavior of cavities operating under pure Kerr effect, theoretical investigations of coherent excitation of a semiconductor microcavity operating under optical Kerr, two-photon absorption (TPA), free carrier refraction (FCR) and free carrier absorption effects have been performed in [18]. In the case of silicon-based microcavities, the optical resonance mainly experiences a frequency blue-shift driven by the refractive index variation induced by free carriers generated by TPA. By delaying blue spectral components, corresponding to a positive linear chirp, it is shown that the benefit of light localization can be maintained throughout the pulsed excitation despite the cavity resonance dynamic frequency shift.

Hereafter, we report the very first experimental demonstration of coherent excitation of a nonlinear microcavity, leading to an enhanced intra-cavity nonlinear interaction. Based on the simulations conducted in [18], we investigate the nonlinear behavior of a silicon-based microcavity coherently excited with tailored positively chirped pulses. For a fixed energy, an increase of up to a factor 2.5 of the carrier density generated inside the cavity by TPA is demonstrated

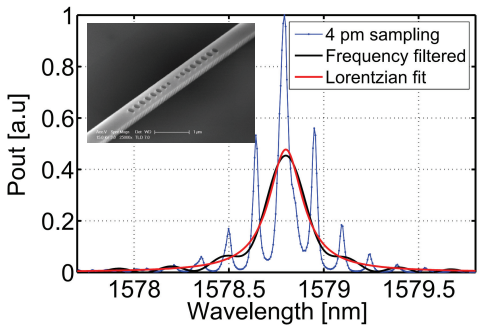

Fig. 1. Linear transmission measurement of the Fabry-Perot type microcavity (blue solid line). The Lorentzian fit of the low-pass filtered linear transmission (black line) plotted in red solid line gives a quality factor $Q = 7275$. Inset: SEM picture of the Silicon microcavity made of two-symmetric Bragg mirrors engraved on a SOI ridge waveguide.

in comparison with Fourier transform limited pulses and negatively chirped counterpart. In addition, we show an enhanced nonlinear interaction allowing to induce a very large frequency blue-shift of the cavity resonance reaching 19 times the linear cavity linewidth. Such a blue-shift is achieved in a silicon microcavity with a Q factor close to 8 000, which is excited by a rectangular spectral shape pulse with a linewidth equal to 6.5 nm, or 30 times the bandwidth of the cold cavity. This result highlights the interest of such a coherent excitation to manipulate the optical bandwidth and the nonlinear dynamics of optical cavities, which could address future trends in the development of integrated optical functions.

2. SOI microcavity

We chose to experimentally investigate the coherent excitation in a Fabry-Perot type microcavity engraved on a Silicon-On-Insulator (SOI) ridge waveguide, commonly known as photonic crystal nanobeam resonator. The cavity geometry is based on two-symmetric tapered Bragg mirrors [19] engraved on a 260×520 nm^2 SOI ridge waveguide, which offers small modal volume and quality factors Q of few thousands, compatible with few picoseconds pulse duration. The high-reflectivity mirrors have been designed with Bloch-mode-engineering concepts [20]. They consist in a taper section with 4 holes and a periodic section made of 4 holes with a 200 nm diameter and a 370 nm periodicity constant. The parameters for the taper section have been optimized in order to achieve a quality factor close to 8000. The taper hole diameters are 130, 160, 190 and 200 nm with the center-to-center hole distances set to 320, 340, 360 and 370 nm. For achieving this design, three-dimensional (3D) numerical calculations of the mirror reflectivity have been performed with the aperiodic Fourier modal method (a-FMM) [21]. The distance between the centers of the two-inner holes of the cavity is set to 450 nm in order to localize the cavity resonance nearby $\lambda = 1580$ nm. Using a 3D FDTD simulation, the calculated modal volume of the designed cavity is $V = 0.8(\lambda/n)^3$, with $n = 3.48$ the refractive index of silicon.

A SEM picture of the fabricated cavity is shown in the inset of Fig. 1. The SOI wafers have been masked by a ZEP-520A resist and the samples have been written using e-beam lithography (80 kV Nanobeam Ltd. nb4 system) followed by an inductive coupling plasma reactive ion etching process using SF6 gas. TE-polarized light delivered by a tunable external cavity laser diode is injected into the access ridge waveguide by using a micro-lensed fiber connected to a polarization-maintaining single mode fibre. The transmitted light is collimated using a microscope objective followed by a TE polarizer, and sent to a sensitive power-meter. As expected

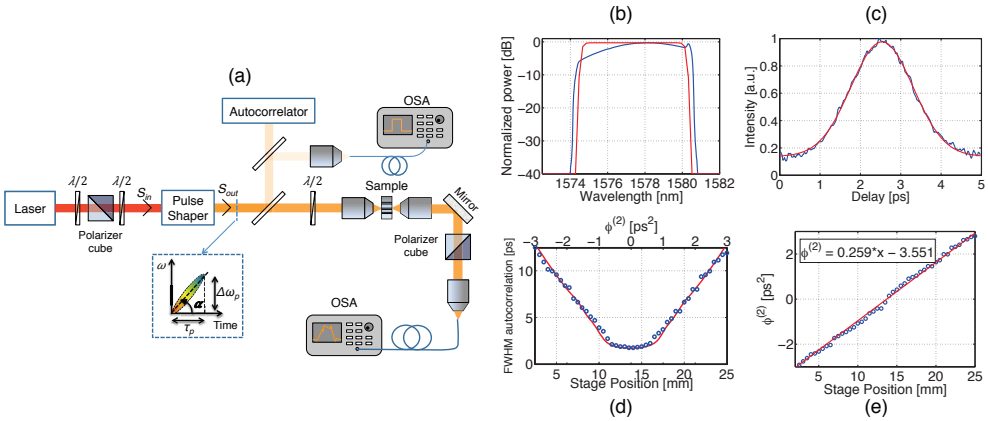

Fig. 2. (a) Experimental set-up where femtosecond pulses of an Er-doped amplifier fiber laser are sent into a grating-based pulse shaper prior to their injection into the sample by means of a microscope objective. (b) Measured optical spectrum of the shaped pulse. (c) Measured (blue line) and simulated (red line) autocorrelation traces of the shaped pulse for $\phi^{(2)} = 0$. (d) Evolution of the full width at half maximum (FWHM) of the autocorrelation traces recorded for different stage positions of the pulse shaper (open circles) and comparison with the calculated values for a linearly chirped rectangular shape pulse spectrum (red line). (e) Relation between the dispersion coefficient and the stage position (open circles) with a linear fit (red line).

from the simulations, the linear transmission measured by scanning the laser wavelength between 1530 and 1600 nm exhibits one peak shown in Fig. 1. The oscillations that are superimposed on the peak originate from the Fabry-Perot effects occurring between the cleaved facets of the device and the cavity mirrors. The 0.14 nm oscillation periodicity is in agreement with the Free-Spectral-Range for a 2.5 mm long cavity, considering that the cavity is situated at the middle of the 5 mm long waveguide. The microcavity peak transmission plotted in black line in Fig. 1 is obtained following low-pass filtering of the Fourier components of the recorded transmission. The Lorentzian fit, red line in Fig. 1, gives a cavity resonance located at 1578.8 nm with a full width at half maximum (FWHM) of $\Delta\lambda_0$ =0.217 nm. The quality factor of the microcavity is estimated to $Q = 7275$, close to the expected value, with a related photon lifetime $\tau_c = Q/\omega$ equal to 6 ps.

Because the experiment consists in evidencing different spectral transmission behaviors of the cavity as a function of input linear chirp of the excitation pulse, the dispersion of the access waveguides must be taken into account. If we consider a 0.1 μm^2 size SOI ridge waveguide, the second-order dispersion coefficient for a TE polarized mode is about $\beta_2 = 1$ ps^2/m [22]. For the shortest pulse duration $T_0 = 1$ ps that will be considered in the following, we verify that this dispersion effect can be neglected since the dispersion length $L_D = T_0^2/|\beta_2|$ equal to 0.5 m is much longer than the few millimeters waveguide length.

3. Pulse parameters

Using the linear parameters of the microcavity, we are now able to proceed with the determination of the shaped pulse parameters that are needed in order to demonstrate the coherent excitation of the microcavity under the nonlinear regime. The experimental set-up scheme shown in Fig. 2(a) consists in controlling, by means of a pulse shaper, the spectral phase relationship and linewidth of pulses delivered by a laser prior to their injection inside the mi-

crocavity. In nonlinear regime, the injected pulses induce a refractive index variation $\Delta n(t)$ of the intra-cavity material, which dynamically modifies the cavity resonance through the relation $\Delta\omega(t)/\omega_0 = -\Delta n(t)/n$. By controlling the spectral phase relationship of the pulse, we seek the instantaneous pulse frequency to follow the cavity resonance drift and to maintain a resonant excitation of the cavity throughout the pulse duration. In such a condition, the cavity is expected to experience a larger frequency shift, which would demonstrate the coherent excitation of a nonlinear cavity and its ability to control its nonlinear behavior.

For a silicon microcavity excited with a few ps pulse duration and at a low repetition time around 20 ns, the nonlinear refractive index variation is predominantly governed by the free-carrier density $N(t)$ generated by two-photon absorption (TPA) [18]. Anticipating that the carrier lifetime is much longer than the cavity photon lifetime, the cavity frequency shift follows the time integral relation $\Delta\omega(t)/\omega_0 = -\sigma_r N(t)/n = -\frac{\sigma_r}{n}\int_{-\infty}^{t}\frac{\beta_{TPA}}{2\hbar\omega_0}\left(\frac{c|u(\tau)|^2}{nV}\right)^2 \mathrm{d}\tau$, which depends on the intra-cavity pulse energy $|u(t)|^2$, the effective volume of the free-carriers σ_r and the TPA coefficient β_{TPA}. This relation shows that the cavity resonance exhibits, for a square temporal pulse shape, a linear blue shift with time and $\Delta\omega(t) \simeq \alpha t$ with α the chirp parameter of the nonlinear cavity resonance. We now assess pulse parameters that are optimal to coherently excite a cavity exhibiting this resonance frequency shift, under the square temporal shape approximation. An order of magnitude for the optimal amount of second-order phase and energy can be simply calculated by setting a target value for the cavity frequency shift $\Delta\omega_p$ covered during the pulse duration τ_p. The target we seek in this article would be to reach a nonlinear shift equal to 30 times the linear cavity linewidth, meaning that $\Delta\omega_p = 30\ \omega/Q$. Under a pulse duration equal to the cavity photon lifetime $\tau_p = \tau_c = Q/\omega$, the dispersion coefficient value is estimated, through $\phi^{(2)} = \tau_p/\Delta\omega_p = Q^2/(30\ \omega^2)$, to a value of +1.3 ps^2. The amount of energy required to reach such a blue shift range, or equivalently the amount of free-carrier density to be generated inside the cavity, are obtained by using the temporal square pulse approximation that leads to $|u|^2 = -\frac{nV}{c}\sqrt{\frac{n\,2\hbar\Delta\omega_p}{\sigma_r\beta_{TPA}\tau_p}}$. This corresponds to a reasonable energy value of 0.4 pJ. For all forthcoming estimations, the following nonlinear parameters $\beta_{TPA} = 0.8$ cm/GW and $\sigma_r = -1.35\times10^{-27}$ m^3 have been considered for silicon [23].

4. Experimental set-up

We are now able to design the pulse shaper used to control the spectral shape of initially Fourier transform-limited 150 fs pulses delivered by a mode-locked erbium-doped fibre laser at a repetition rate of $F = 50$ MHz. It should include the possibility to adjust the outgoing pulse spectral linewidth and chirp coefficient. To show the strong dependence of the nonlinear behavior of the cavity with the spectral phase relationship of the pulse, we have designed a pulse shaper enabling to cover a dispersion coefficient range of few ps^2 with the possibility to select either a positive or a negative value. With these constraints, we chose to build a grating-based pulse stretcher that includes an optical lens to modify the dispersion sign [24]. A detailed description of the pulse shaper is given in Appendix A, which comprised an optical grating, an optical lens, a mirror and a roof prism to fold the set-up. The spectral bandwidth of the pulse is adjusted by means of a slit. The dispersion coefficient $\phi^{(2)}$ is controlled by translating the distance between the lens-mirror-slit set-up and the grating using a translation stage.

The pulse spectrum of the outgoing pulse is plotted in blue curve in Fig. 2(b) showing an almost rectangular-shaped spectrum with a bandwidth set to 6.5 nm, which matches with the target nonlinear cavity shift $\Delta\omega_p = 30\ \omega/Q$. In order to characterize our pulse shaper, the outgoing pulse duration has been measured with an autocorrelator for different stage positions. The full width at half maximum (FWHM) of the autocorrelation traces recorded for the stage positions varying over 25 mm is plotted with open circles in Fig. 2(d). The symmetric shape

of the curve shows that the pulses do not suffer from any nonlinear phase distorsion that could have been introduced in the fiber laser module. In order to determine the relation between the stage position and the dispersion coefficient $\phi^{(2)}$, the curve has been fitted with the numerically calculated auto-correlation traces of a linearly chirped pulse with a 32^{nd} order supergaussian spectral shape. The fitting curve is reported in the Fig. 2(d) with red solid line, which is achieved with the 5.7 nm width spectral shape plotted with red curve in Fig. 2(b). The perfect adjustment between the measured and the expected pulse durations proves that the pulses we generate respect the Fourier limit. Especially, for $\phi^{(2)} = 0$ ps^2, the measured and simulated autocorrelation traces plotted in Fig. 2(c), respectively in blue and red lines, show a very good overlap with an autocorrelation pulse duration equals to 2 ps, which corresponds to a pulse duration of 1.1 ps. The little discrepancy between experimental and simulated spectral pulse linewidths can be explained by the slight difference in their spectral shape. We are now able to connect the stage position with the dispersion coefficient as shown in the Fig. 2(e), which exhibits a linear dependence with a slope equal to 2.59 ± 0.02 ps^2/cm. The accuracy is limited by that of the stage position measurement estimated to 100 μm.

Following the characterization of the pulse shaper, we have tested the injection of the shaped pulses inside a ridge waveguide that is adjacent to the cavity and has exactly the same cross-section and length. Two identical optical microscopes ($\times 60$) are used respectively to inject the beam coming from the pulse shaper inside the waveguide, and to collimate the outgoing light prior to its injection into a single mode fiber connected to an optical spectrum analyzer (OSA). A half-wave plate is used at the entrance to select the TE-polarized guided mode, while a polarizing cube is placed at the output to filter undesired polarization states. We have verified that the coupling loss dependence with the stage position of the pulse shaper remains low with a variation of about 8 % in the transmission power (see Appendix B for details).

In order to evaluate the coupling efficiencies, and finally the pulse energy injected inside the waveguide, we have characterized pulse transmission in nonlinear regime by recording a set of transmission spectra for increasing averaged input power P_{in} up to 9 mW with $\phi^{(2)} = 0$ ps^2. The analysis of the nonlinear transmission curve, which is governed by the two-photon absorption effect, allows to estimate the coupling efficiency to 2.8 % and to measure the maximum pulse energy of the injected pulses to 5 pJ, which is sufficient to reach the 0.4 pJ preliminary calculated in section 3 (see Appendix B for details).

5. Nonlinear behavior of a coherently excited microcavity

We next study the nonlinear behavior of the SOI microcavity, presented in section 2, under a coherent excitation in order to demonstrate that a proper control on the spectral shape of the excited pulse enables to control the intra-cavity nonlinear interaction. This experimental study is performed by measuring the evolution of the transmission spectra for different dispersion coefficients $\phi^{(2)}$ at a fixed incident energy.

The angular position of the grating in the pulse shaper is adjusted to deliver pulses centered around 1579 nm, the central wavelength of the microcavity (see Fig. 1). The incident average pump power is measured equal to $P_{in} = 6.8$ mW and its optical spectrum is plotted on top of Fig. 3 in red line. At very low input power, the measured transmission spectrum is plotted in Fig. 3 in grey line ($\times 20$), which coincides with the linear transmission of the microcavity previously depicted in Fig. 1. While the spectrum of the incident pulse is 30 times larger than the linear cavity resonance, with a spectral linewidth set to 6.5 nm, only the spectral components that coincide with the cavity resonance are transmitted.

For a fixed average power P_{in} =6.8 mW, the transmission spectra recorded for dispersion coefficients varying between -3 to $+3.5$ ps^2 are plotted in Fig. 3. One can first notice that all the transmission spectra are blue-shifted with respect to the linear cavity resonance. Considering a

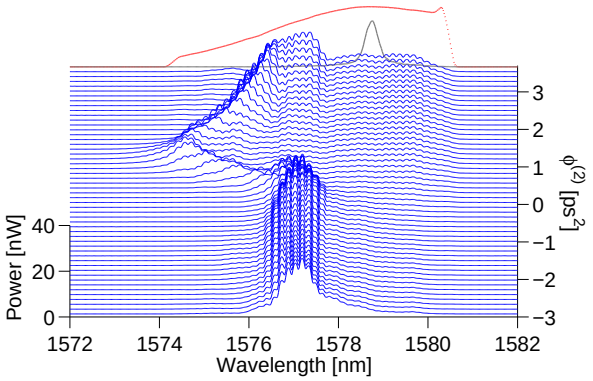

Fig. 3. Evolution of the transmission spectra of the cavity measured with varying the chirped pulse excitation from $\phi^{(2)} = -3$ to +3.5 ps^2. The spectral linewidth of the incident pulse is plotted in red line. The transmission spectrum measured at low incident power is shown in grey line.

Fabry-Perot type microcavity, a frequency shift in the transmission spectra coincides to that of the cavity resonance, which in our case is driven by the refractive index change induced by the free carriers generated by TPA. This nonlinear effect has been already employed to realize all-optical switches on SOI microcavities [5, 25]. Although the transmission spectra remain almost unchanged for negative chirps, they clearly exhibit an increasing blue-shifted content for values of $\phi^{(2)}$ varying from 0 to +1.2 ps^2. Beyond this value, the blue shift slightly decreases.

To give physical insights in the nonlinear cavity behavior, we compare in Fig. 4 the transmission spectra, both in linear scale (a) and dBm scale (b), achieved with $\phi^{(2)} = 0$ ps^2 and with two opposite chirps + and -1.2 ps^2. Under a Fourier-Transform limited pulse excitation, at zero dispersion, the cavity resonance exhibits a 1.6 nm blue-shift as shown with the blue line spectrum. In the time domain, the pulse duration, which is about 1.1 ps, is shorter than the cavity photon lifetime and the cavity resonance is excited in a slightly transient regime. In contrast, the two opposite chirped pulses ± 1.2 ps^2 exhibit an autocorrelation pulse duration of 8 ps, giving a pulse duration (5.7 ps) equals to the cavity photon lifetime. Compared with the -1.2 ps^2 chirped pulses (green curve), the transmission spectrum for $\phi^{(2)} = +1.2$ ps^2 (red curve) leads to a larger blue-shift and a remarkably broader transmission spectrum, which almost matches the input pulse bandwidth. In comparison, the blue-shift achieved with $\phi^{(2)} = -1.2$ ps^2 coincides with that obtained for the FT-limited pulses $\phi^{(2)} = 0$ ps^2. Whereas the two pulse excitations ± 1.2 ps^2 give the same pulse duration, they differ in the sign of their spectral phase relation. Under the positive chirp case, the cavity is first excited by the red components of the pulse. Although the red side of the pulse spectrum is detuned from the centered wavelength of the cavity resonance, the transmission around 1580 nm is not null, meaning that the cavity resonance starts to store some energy and to shift towards the blue. Owing to the linear time-frequency relation of the pulse, the coupling efficiency to the drifted resonance can be maintained, increasing further the blue-shift extension compared with the negative chirped pulse.

The unambiguous differences between the transmission spectra for the two chirped pulses + and -1.2 ps^2 signify that the nonlinear behavior taking place inside the microcavity clearly depends on the delay between the spectral components of the excited pulse. We claim that the +1.2 ps^2 chirped pulse excitation coincides with the situation where the delay between the

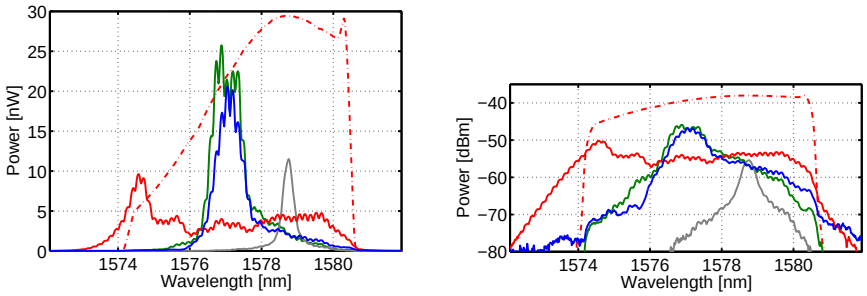

Fig. 4. Measured incident (dashed line) and transmission spectra, plotted in linear scale (a) and in dBm scale (b) at low energy (grey line, $\times 5$ in linear scale) and at 5pJ incident energy for various chirped pulse excitation: Fourier-Transform limited pulses (blue line), $\phi^{(2)} = -1.2$ ps^2 (green curve), $\phi^{(2)} = +1.2$ ps^2 (red curve).

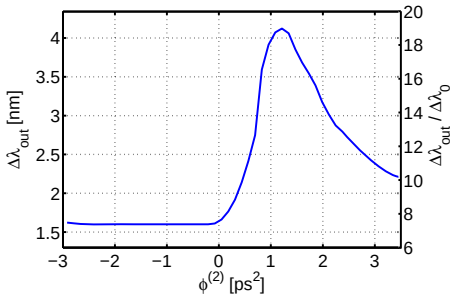

Fig. 5. Measured cavity blue-shift achieved for the chirp coefficients $\phi^{(2)}$ reported in Fig. 3. The shift in wavelength is measured with respect to the linear cavity resonance.

spectral components of the pulse matches the instantaneous cavity frequency drift, which, with a good approximation, follows a linear time variation [18].

The broader transmission spectrum, and equivalently the larger spectral blue-shift of the resonance achieved with the positively chirped pulse, are necessarily assisted by a higher carrier density generation and prove an enhanced nonlinear interaction between the pulse and the intra-cavity material, i.e. a better energy transfer between the incident pulse and the cavity resonance. In Fig. 5, the measured nonlinear cavity blue-shift $\Delta\lambda_{out}$ in wavelength (with respect to the linear cavity resonance) is extracted from Fig. 3. As previously said, the cavity blue-shift is maintained at a fixed value $\Delta\lambda_{out} = 1.6$ nm for negative dispersion coefficients, which tends to signify that the amount of energy transferred from the incident pulse to the microcavity remains unchanged. On the other hand, the cavity blue-shift behavior towards $\phi^{(2)} > 0$ shows an increase by a factor 2.5 between 0 and +1.2 ps^2, meaning that TPA generated carrier density is 2.5 times higher. For higher dispersion coefficients, the blue-shift experienced by the cavity resonance decreases. A better transfer of energy between the incident pulse and the intra-cavity material is achieved under the $\phi^{(2)} =$+1.2 ps^2 excitation pulse, leading to a enhanced nonlinear interaction.

To compare with the preliminary values we targeted in Section 3, the right axis of the graph in Fig. 5 reports the ratio between the achieved experimental blue-shift $\Delta\lambda_{out}$ and the cavity resonance linewidth $\Delta\lambda_0$ measured in linear regime. While the cavity blue-shift is constantly equal to $\Delta\lambda_{out} = 7 \times \Delta\lambda_0$ for $\phi^{(2)} < 0$, it reaches $\Delta\lambda_{out} = 19 \times \Delta\lambda_0$ at $\phi^{(2)} =$+1.2 ps^2, which is

very close to the dispersion coefficient previously anticipated in order to reach a cavity blue-shift of $30 \times \Delta\lambda_0$. Note that, experimentally, the red side of the pulse spectrum is red detuned from the linear cavity resonance by 2 nm, or equivalently by $10 \times \Delta\lambda_0$, which is not counted in the evaluation of $\Delta\lambda_{out}$ in Fig. 5.

Finally, the amount of absorbed energy achieved for $\phi^{(2)} = +1.2$ ps^2 can be estimated by substituting the frequency blue shift $\Delta\lambda_{out} = 4.1$ nm into the relation given at the end of Section 3, which gives an estimated energy of 0.3 pJ for a refractive index variation $\Delta n/n = \Delta\lambda_{out}/\lambda = 2.5 \times 10^{-3}$. This variation is about one order of magnitude higher than the values reported in [25] in a SOI ring cavity with a quality factor of 3000, or in [26] in a SOI photonic crystal cavity with $Q = 7000$.

6. Simulations

We next conduct a preliminary simulation of the nonlinear behavior of our cavity using the coupled mode theory [18,23], which describes the time evolution of the intra-cavity field amplitude $u(t)$ and the free-carrier density $N(t)$:

$$\begin{aligned} \frac{\mathrm{d}u}{\mathrm{d}t} &= i\,\omega_0 \left(1 - \frac{n_2 c}{n^2 V_\mathrm{K}}|u(t)|^2 - \frac{\sigma_r}{n}N(t)\right) u(t) \\ &\quad - \left(\frac{\omega_0}{2Q} + \frac{\beta_\mathrm{TPA} c^2}{2n^2 V_\mathrm{K}}|u(t)|^2 + \frac{\sigma_a c}{2n}N(t)\right) u(t) + \sqrt{\frac{\omega_0}{Q_e}}\, s_{inc}(t) \qquad (1) \\ \frac{\mathrm{d}N}{\mathrm{d}t} &= -\frac{1}{\tau_c}N(t) + \frac{\beta_\mathrm{TPA}}{2\hbar\omega_0}\frac{c^2}{n^2 V_\mathrm{FC}^2}|u(t)|^4, \qquad (2) \end{aligned}$$

where $s_{inc}(t)$ is the incident pulse field defined as $|s_{inc}(t)|^2 = P_{inc}(t)$, with $P_{inc}(t)$ the incident pulse peak power, ω_0 the angular frequency of the linear cavity, c the speed of light in vacuum, and $\hbar$ the reduced Planck constant. The first term of the right hand side of Eq. 1 describes the modification of the linear cavity resonance ω_0 under the refractive index variation governed by both the Kerr effect, with n_2 the nonlinear refractive index of Silicon, and the free-carrier refraction effect proportional to $N(t)$. The second term refers to the energy decay time in the cavity related to the Q factor in the linear regime, which is modified by the TPA effect and the free-carrier absorption (FCA) effect, with σ_a the FCA cross section of Silicon. The free-carrier density $N(t)$ evolution, described by Eq. 2, accounts for the lifetime τ_c of the free-carriers and for a generation term induced by TPA effect. The expressions for the effective volumes related to optical Kerr and TPA effects V_K and free-carrier effects V_FC are derived from [27], and calculated by means of FDTD simulations, which give $V_\mathrm{K} = 2.3(\lambda/n)^3$ and $V_\mathrm{FC} = 1.7(\lambda/n)^3$. The linear parameters of the cavity are determined by the simulations initially performed in Section 2 and set to $Q = 7\,900$ and $Q_e = 8\,500$, which is related to the coupling between the incident field and the cavity. To complete the model, the nonlinear parameters of Silicon are set to: $n_2 = 4.4 \times 10^{-18}$ m^2/W, $\beta_{TPA} = 8 \times 10^{-12}$ m/W, $\sigma_r = -1.35 \times 10^{-27}$ m^3, $\sigma_a = 14.5 \times 10^{-22}$ m^2, and the carrier lifetime was set to $\tau_c = 0.4$ ns [23]. As discussed in [18], the nonlinear contributions issued from thermal effects can be neglected in our experiment.

Following the measurements of the optical spectra at the output of the SOI ridge waveguide reported in Fig. 8(b) in Appendix B, the free carrier nonlinear effects occurring in the access waveguide are negligible as we do not observe any significant blue-shift. However, our model includes the accumulated nonlinear phase due to optical Kerr and the TPA power depletion that are experienced by the incident pulse into the access waveguide prior to the microcavity excitation. As in the experience, the microcavity is located at 2.5 mm from the input facet.

For the simulations, the input spectral shape in intensity is taken equal to the 32$^{\mathrm{nd}}$ order supergaussian shape plotted in Fig. 2(b), whose 5.7 nm linewidth gives an autocorrelation trace

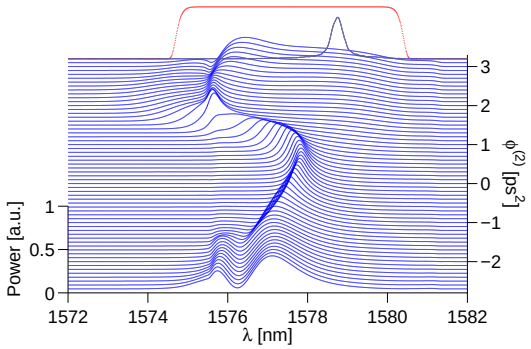

Fig. 6. Simulated transmission spectra of the cavity under chirped pulse excitations varying from $\phi^{(2)} = -3$ to +3.5 ps^2. The spectral linewidth of the incident pulse is plotted in red line. The transmission spectrum calculated at low incident power is shown in grey line.

that matches with the experimental trace (as shown in Fig. 2(c)). The injected peak power is set to 4.5 W coinciding with the pulse energy of 5 pJ estimated in Appendix B from the nonlinear transmission of the SOI ridge waveguide. The transmitted spectra calculated under various chirped pulse excitations, with dispersion coefficients varying between -3 to $+3.5$ ps^2, is shown in Fig. 6. Despite a slight discrepancy, the simulated spectra are in very good agreement with the experimental results given in Fig. 3. Like in the experiment, the simulated transmission spectra exhibit a larger blue-shift for positive $\phi^{(2)}$, with a maximum value reached at $\phi^{(2)} = +1.7$ ps^2 that is very close to the reported experimental value of +1.2 ps^2. Beyond this value, the frequency shift of the cavity resonance decreases like for the measured spectra. Although the simulated spectra for negative chirp do not perfectly match the measurements, they clearly show a lower blue-shift compared to the positive $\phi^{(2)}$ spectra. The nonlinear behavior of the SOI microcavity under a coherent excitation experimentally reported in this article, is confirmed by our preliminary simulations that reproduce the general trends for the transmission spectra. In order to further precise our model, additional simulation work is under progress to better fit with the experimental behavior taking into account, for instance the actual spectral shape of the input pulse.

7. Conclusion

We have experimentally demonstrated for the first time, the coherent excitation of a nonlinear SOI microcavity. By controlling the linear chirp of the excitation pulse, an enhanced nonlinear interaction between the pulse and the intra-cavity silicon material is experimentally demonstrated. Compared with a Fourier-transform limited pulse of equal energy, positively chirped pulse excitation enables to increase the free carrier density generated by TPA by up to a factor of 2.5. It is accompanied by a large frequency blue-shift of the cavity resonance reaching 19 times the linear cavity linewidth, corresponding to a refractive index variation $\Delta n/n = 2.6\,10^{-3}$. These experimental results were verified using a coupled mode theory model that includes all Silicon nonlinearities.

This result highlights the interest of such a coherent excitation to manipulate the optical bandwidth as the spectral pulse linewidth used to excite the silicon microcavity, with a Q factor close to 8 000, is 30 times larger than the bandwidth of the cold cavity. Although our experimental results do not include temporal measurements, one has to remind that the variations

in the transmission spectra are necessarily accompanied by differences in the intra-cavity field dynamics, as illustrated in [18] for gaussian shape pulse excitations, underlying the interest of coherent excitation in the purpose of controlling the nonlinear dynamics of optical cavities or optical devices.

Thanks to a physical analysis of the nonlinear behavior of the microcavity, we were able to predetermine the pulse shape, in particular the spectral phase relationship approximated to a positively linear chirp. Such an approach refers to an open-loop coherent control scheme [14] that do not require any experimental feedback. In contrary, close-loop scheme could be envisaged to excite optical resonators, as it is routinely achieved for atomic and molecular resonances [28], which could be an interesting method to characterize nonlinear dynamics of optical resonators and nonlinear parameters of intra-cavity materials.

Finally, this illustration in the capability to manipulate the optical bandwidth and the nonlinear dynamics of a cavity by means of a coherent excitation could be applied to more complex structures like coupled cavities. This coherent control of on-chip resonator may open new routes for low-power optical switches [2] and all-optical memories [29].

Appendix A: Pulse shaper design

As shown in Fig. 7, the pulse shaper comprises a diffraction grating followed by a doublet lens and a mirror located at the focal plane. A roof prism is used to fold the system. The spectral bandwidth of the pulses is adjusted by means of a slit set in front of the mirror. This set-up is actually the folded version of the 4-f set-up introduced by C. Froehly et al. in [30]. The 2nd order dispersion coefficient $\phi^{(2)}$ is introduced by varying the distance L between the lens-mirror-slit set-up and the grating around the focal distance f using a stage position. By doing so, a curvature of the front wave is introduced at the mirror location with a sign varying for the distance L set towards the focal distance. Because the spatial distribution of the beam at the mirror mimics its spectral distribution, the wave front distorsion equivalently introduces a spectral phase of the form $e^{\imath\phi^{(2)}\omega^2}$. By either using a ray-optics based calculation or the more complete theoretical description given in [24], one can show that $\phi^{(2)} = \frac{-8\pi^2 c(L-f)}{\Lambda^2\omega^3\cos^2\theta_R}$, where Λ and θ_R are respectively the grating period and the first-order diffraction angle. It is worth noting that this formula is similar to the dispersion achieved with a pair of gratings set-up separated by a distance g (instead of $L-f$) [31]. The strong difference being that the sign of the dispersion is always negative in the latter, whereas it can be adjusted in the former through the sign of the quantity $L-f$.

We selected a 1200 lines/mm grating for which we measured a diffraction efficiency in the Littrow configuration higher than 85 % in the spectral range 1520-1580 nm and for a TE-polarized light. The doublet lens has a focal distance $f = 20$ cm. Following these parameters, few ps^2 dispersion coefficients are obtained by varying the distance L towards the focal plane by a quantity around 10 mm.

Appendix B: Nonlinear characterization of a SOI ridge waveguide

Prior to the nonlinear characterization of a 5 mm long SOI ridge waveguide, we first verify the coupling loss dependence with the stage position of the pulse shaper by recording 25 optical spectra at a fixed low power but for different dispersion coefficients. The superimposed traces of the transmission spectra measured for $\phi^{(2)}$ comprised between +3 and -3 ps^2 are plotted in Fig. 8(a). Despite the stage translation over 25 mm, one can see that the variation on the coupling efficiency remains low with a variation of about 8 % in the transmission power. One can also note that the optical spectrum shapes are similar, signifying that the beam delivered by the pulse shaper does not suffer from any spatial chirp effect.

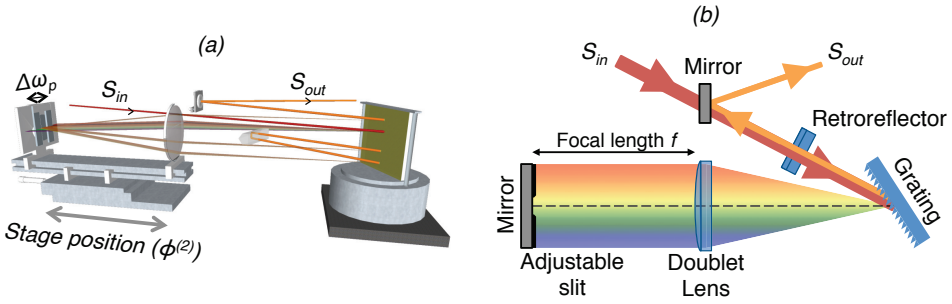

Fig. 7. Pulse shaper scheme: 3D (a) and top-view (b). It comprises a diffraction grating, a doublet lens, a mirror located a the focal plane of the lens and a roof prism. The slit set in front of the mirror serves to adjust the spectral linewidth of the outgoing pulse. The 2nd order dispersion coefficient of the outgoing pulse is introduced by translating the lens-mirror-slit set-up using a stage position.

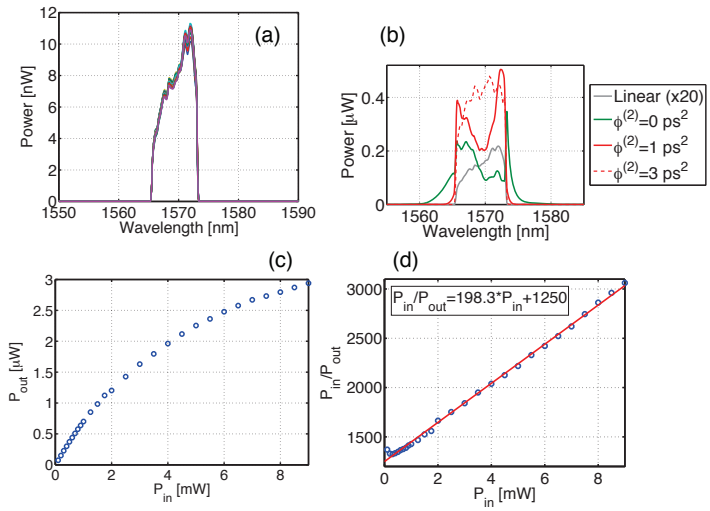

Fig. 8. (a) Superimposed traces of 25 transmission spectra measured through a SOI ridge waveguide, at low input power, and for $\phi^{(2)}$ comprised between +3 and -3 ps^2. (b) Transmission spectra measured at low power (grey line, 20 times magnified) and at P_{in} =9 mW for $\phi^{(2)} = 0$ (green line), 1 (red solid line) and 3 ps^2 (red dashed line). For increasing input power, variation of P_{out} (c) and P_{in}/P_{out} (d) with the related linear fit (red line).

Next, we record a set of transmission spectra for increasing averaged input power P_{in} up to 9 mW with $\phi^{(2)} = 0$ ps^2. Our objective is to evaluate the coupling efficiencies from the analysis of the nonlinear transmission. For each optical spectrum, we calculate the average output power P_{out} that is related to the peak intensity inside the waveguide $I(L_g)$ by $P_{out}/(A_{eff}\tau_P F) = \kappa_{out} I(L_g)$, with κ_{out} the whole output coupling efficiency from the exit facet of the waveguide to the OSA. Similarly, the injected peak intensity $I(0)$ is connected to the input power P_{in} through the relation $I(0) = \kappa_{in} P_{in}/(A_{eff}\tau_P F)$, with κ_{in} the input coupling efficiency. The measured P_{out} for increasing P_{in} plotted in Fig. 8(c) deviates from a linear variation, attesting the presence of nonlinear absorption. Figure 8(d) reports the variation of P_{in}/P_{out} for increasing input power, which follows a linear variation in accordance with the expected non-

linear transmission governed by the two-photon absorption effect. The experimental data can be fitted by the relation [32, 33] $P_{in}/P_{out} = a + bP_{in} = 1/\kappa + \kappa_{in}\beta_{TPA}L_{eff}P_{in}/(\kappa A_{eff}\tau_P F)$, which accounts for the effective waveguide length $L_{eff} = \left(1 - e^{-\alpha_g L_g}\right)/\alpha_g$, with α_g the linear attenuation, and for the total linear losses $\kappa = \kappa_{in}\kappa_{out}e^{-\alpha_g L_g}$. The linear attenuation of the waveguide has been measured equal to $\alpha_g = 0.2$ cm^{-1} through the analysis of the modulation depth of the Fabry-Perot fringes recorded on a spectral transmission of the waveguide. The linear fit plotted with a solid red line in Fig. 8(d) gives $a = 1250$ and $b = 198.3$ mW^{-1}, enabling to estimate the coupling efficiency $\kappa_{in} = b/a \times A_{eff}\tau_P F/(\beta_{TPA}L_{eff}) = 2.8\%$ taking $\tau_p = 1.1$ ps the pulse duration measured for $\phi^{(2)} = 0$ ps^2 . Finally, we can have access to the pulse energy injected inside the waveguide, its maximum value is estimated to 5 pJ. Under such a condition, it is worth noting that the transmission spectrum depicted in Fig. 8(b) in green solid line exhibits a broadening effect by comparing with the transmission spectrum recorded at low input power (grey solid line). The symmetric tails located at the two sides of the spectrum signifies that the pulses mainly undergo self-phase modulation effect through the optical Kerr effect. Now, this broadening tends to disappear when we increase the dispersion coefficient as can be seen from the Fig. 8(b) where the two transmission spectra for $\phi^{(2)} = 1$ and 3 ps^2 are reported respectively in solid and dashed red lines, as the pulse duration increases and the peak power decreases.

Acknowledgments

The authors thank Robert Frey, Gilles Pauliat and Philippe Lalanne for helpful discussions and highly valuable comments.